Hindawi
Modelling and Simulation in Engineering
Volume 2020, Article ID 3862624, 22 pages
https://doi.org/10.1155/2020/3862624

Research Article

Thermohydraulic Performance Improvement in Heat Exchanger Square Duct Inserted with 45° Inclined Square Ring

Amnart Boonloi[1] **and Withada Jedsadaratanachai**[2]

[1]*Department of Mechanical Engineering Technology, College of Industrial Technology, King Mongkut's University of Technology North Bangkok, Bangkok 10800, Thailand*
[2]*Department of Mechanical Engineering, Faculty of Engineering, King Mongkut's Institute of Technology Ladkrabang, Bangkok 10520, Thailand*

Correspondence should be addressed to Withada Jedsadaratanachai; kjwithad@kmitl.ac.th

Received 4 October 2019; Revised 7 December 2019; Accepted 16 December 2019; Published 13 January 2020

Academic Editor: Joseph Virgone

Thermal performance development, heat transfer structure, and flow behavior in the heat exchanger square duct equipped with a 45° inclined square ring are investigated numerically. The effects of flow blockage ratios and spacing ratios for the inclined square ring on fluid flow and heat transfer are considered. The Reynolds number (Re = 100–2000, laminar regime) based on the hydraulic diameter of the square duct is selected for the present work. The numerical domain of the square duct inserted with the 45° inclined square ring is solved with the finite volume method. The SIMPLE algorithm is picked for the numerical investigation. The heat transfer characteristics and flow topologies in the square duct inserted with the inclined square ring are plotted in the numerical report. The heat transfer rate, pressure loss, and efficiency for the square duct placed with the inclined square ring are presented in forms of Nusselt number, friction factor, and thermal enhancement factor, respectively. As the numerical results, it is detected that the heat transfer rate of the heat exchanger square duct inserted with the inclined square ring is around 1.00–10.05 times over the smooth duct with no inclined square ring. Additionally, the maximum thermal enhancement factor for the heat exchanger square duct inserted with the inclined square ring is around 2.84.

1. Introduction

The effort to develop the thermal performance of the heat transfer system in various industries and engineering devices had been considered by many researchers. The improvement of the heat transfer rate and thermal performance in the heat exchanger can be done by two methods. The first method is called "active method." The active method requires additional power, such as vibration, to improve heat transfer rate. The second method is named "passive method." The passive method is to produce the vortex flow to disturb the thermal boundary layer on the heat transfer surface. The passive method is done by installing the vortex generators or turbulators in the heating system. Rib [1–8], baffle [9–13], winglet [14–19], etc., are types of the vortex generators.

The types, configuration, parameter, etc., of the vortex generators had been studied and developed by many researchers. For example, Chamoli et al. [20] numerically investigated the thermal performance augmentation in a circular tube with novel anchor-shaped vortex generators for the Reynolds number around 3000–18,000. They concluded that the heat transfer rate and friction loss for the circular tube with the novel anchor-shaped vortex generators are higher than the plain tube around 2.24–4.56 and 4.01–23.23 times, respectively. They also found that the maximum thermal enhancement factor for the circular tube with the novel anchor-shaped vortex generators is around 1.72. Bartwal et al. [21] reported the heat transfer increment in the heat exchanger by the circular ring with a wire net. They summarized that the

heat transfer in the heat exchanger is greater than the smooth tube around 3.35 times, while the maximum thermal performance is around 2.84. Chamoli et al. [22] presented the thermal performance of a solar air heater placed with the winglet vortex generator. The effects of tip edge ratio and flow attack angle for the winglet on heat transfer, pressure loss, and performance were studied for Re = 3500–16,000. They claimed the winglet vortex generator in the heat exchanger gives the best thermal performance in the range 1.72–2.20. Singh et al. [23] studied the influences of the perforated hollow circular cylinder in a circular tube for Re = 6000–27,000. They found that the perforated hollow circular cylinder in the circular tube provides the heat transfer rate around 150–230% when compared with the smooth tube. Chamoli et al. [24] illustrated the convective heat transfer in a circular tube fitted with perforated vortex generators. The effects of the perforation index and relative pitch length on heat transfer and thermal performance in the tested tube were considered for Re = 3000–21,000. They found that the circular tube with perforated vortex generators provides the maximum thermal enhancement factor around 1.65. The multiobjective shape optimization of a heat exchanger tube fitted with compound inserts was reported by Chamoli et al. [25]. Sawhney et al. [26] experimentally examined the heat transfer and friction factor in a solar air heater duct with wavy delta winglets for the Reynolds number around 4000–17,300. The number of wave and relative longitudinal pitch for the wavy delta winglet was compared. They claimed that the wavy delta winglet in the duct performs the heat transfer rate greater than the plain duct around 223%.

The objective for the present research is to design the vortex generator with the special conditions as follows:

(i) The new design has high effectiveness to increase heat transfer rate in the heat exchanger section

(ii) The installation and maintenance of the vortex generator in the heat exchanger are stable and convenient

(iii) The production of the vortex generator is not complicated

In the present research, the passive method is focused. The inclined square ring (ISR), like the baffle or thin rib, is selected to improve heat transfer rate and performance in the heat exchanger square duct. The parameter of the ISR and placement in the heating duct is investigated numerically in three dimensions. The numerical investigation may help to describe the flow and heat transfer structures in the heating section. The understanding on flow and heat transfer behaviors in the heat exchanger is an important factor for the development of the compact heat exchanger. The numerical study also saves the cost and resource for the studied process when compared with the experimental examination. The numerical results are plotted in terms of flow and heat transfer configurations in the tested section such as temperature contour, Nu_x Contour, and streamlines. The performance analysis in form of Nusselt number, friction factor, and thermal enhancement factor for the heat exchanger square duct equipped with ISR is also concluded.

2. Tested Section with 45° ISR

The computational domain of the heat exchanger square duct inserted with the 45° ISR is plotted in Figure 1. The physical domain of the square duct inserted with the 45° ISR in y-z plane is depicted as Figure 2. The height of the square duct, H, is around 0.05 m. The duct height is equal to the hydraulic diameter or $H = D_h$. The ISRs are inserted in the square duct with single pitch spacing ratio of 1 ($P/H = 1$) in all investigated cases. The ratio between the ISR height, b, and channel height, H, or b/H is varied in the range 0.05–0.30. The spacing between the outer edge of the ISR and the channel wall, s, is varied in terms of spacing ratio or $s/H = 0$–0.30. The air flow rate is presented in the form of Reynolds number. The Reynolds number at the inlet condition around 100–2000 is considered for the current work. The numerical models with the mesh of the heat exchanger square duct inserted with the 45° ISR are illustrated as Figures 3(a) and 3(b) for $s/H = 0$ and 0.20, respectively, at $b/H = 0.20$.

3. Numerical Method

The flow is a laminar regime with the Reynolds number based on the hydraulic diameter. The flow and heat transfer are steady in three dimensions. The tested fluid is set as incompressible flow. The tested fluid is air with the Prandtl number around 0.707 (300 K). The thermal properties of the air are counted to be constant at the average bulk mean temperature. The heat transfer in the force convection mode is considered for the present work, while the radiation and natural convection are ignored. The body force and viscous dissipation are also disregarded. No slip wall condition is applied for all channel surfaces and ISR. The periodic condition [27] on both flow and heat transfer is applied for the inlet and outlet of the computational domain. The ISR is assumed to be an insulator, while the duct walls are set with constant temperature around 310 K. The flow and heat transfer in the heat exchanger duct fitted with the ISR are in fully developed condition [28].

The finite volume with the SIMPLE algorithm is selected to solve the present investigation. The present model is answered by the continuity, the Navier–Stokes equations, and the energy equation, which are illustrated as equations (1)–(3), respectively. The continuity equation, momentum equation, and energy equation are discretized by the power law scheme, power law scheme, and QUICK scheme, respectively. The numerical solutions are considered to be converged when the normalized residual values are less than 10^{-5} for all variables but less than 10^{-9} only for the energy equation.

Continuity equation:

$$\frac{\partial}{\partial x_i}\left(\rho u_i\right) = 0. \tag{1}$$

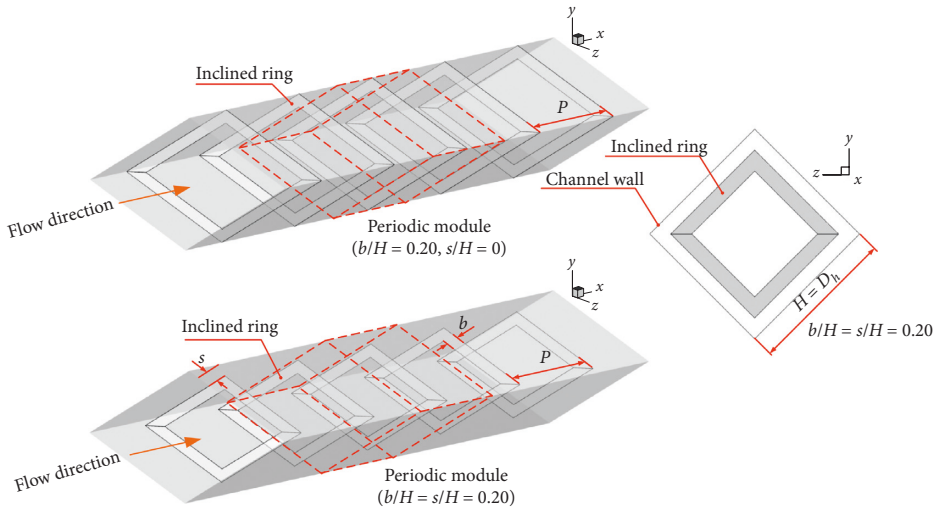

Figure 1: Computational domain of the heat exchanger square duct installed with the 45° ISR.

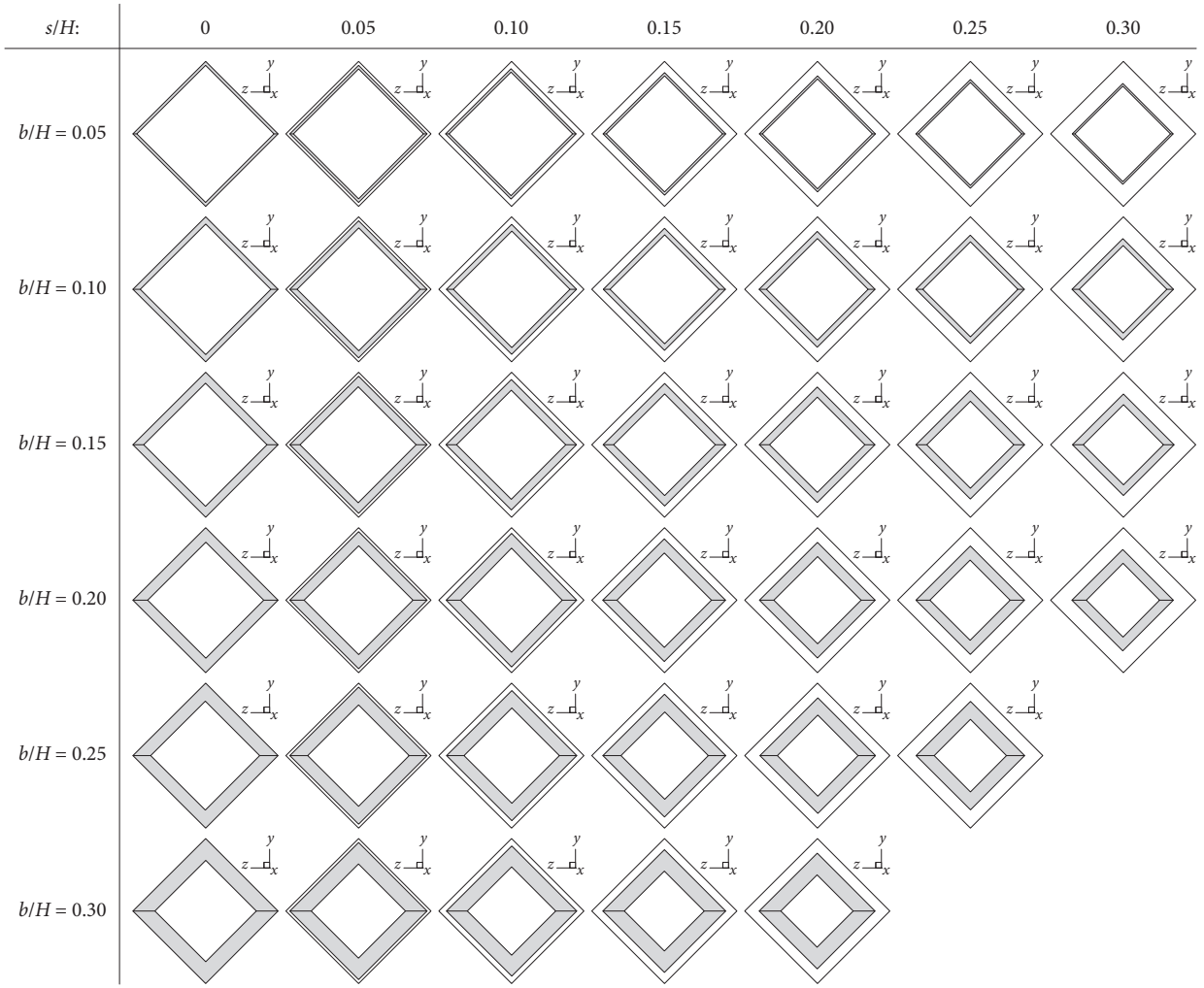

Figure 2: Square duct installed with the 45° ISR in the y-z plane at various cases.

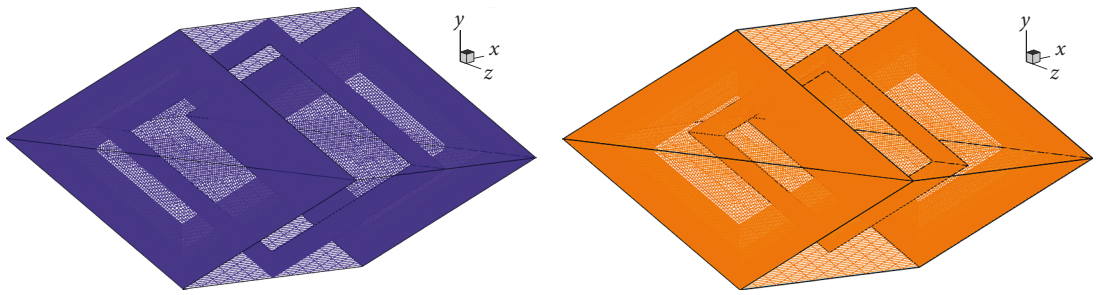

(a) (b)

Figure 3: Computational domain with the mesh of the heat exchanger square duct installed with the 45°ISR for (a) $b/H = 0.20$, $s/H = 0$, and (b) $b/H = s/H = 0.20$.

Momentum equation:

$$\frac{\partial\left(\rho u_i u_j\right)}{\partial x_j} = -\frac{\partial p}{\partial x_i} + \frac{\partial}{\partial x_j}\left[\mu\left(\frac{\partial u_i}{\partial x_j} + \frac{\partial u_j}{\partial x_i}\right)\right]. \tag{2}$$

Energy equation:

$$\frac{\partial}{\partial x_i}\left(\rho u_i T\right) = \frac{\partial}{\partial x_j}\left(\Gamma \frac{\partial T}{\partial x_j}\right), \tag{3}$$

where Γ is the thermal diffusivity and is printed as follows:

$$\Gamma = \frac{\mu}{\mathrm{Pr}}. \tag{4}$$

The tested fluid is offered in terms of the Reynolds number based on the hydraulic diameter of the square duct, D_h. The hydraulic diameter of the square duct is equal to duct height ($D_h = H$). The Reynolds number is written as follows:

$$\mathrm{Re} = \frac{\rho \overline{u} D_h}{\mu}. \tag{5}$$

The pressure loss of the square duct equipped with the 45° ISR is reported in the form of friction factor. ΔP is the pressure drop across the periodic module. The length of the periodic module is presented with L. The friction factor can be determined as follows:

$$f = \frac{(\Delta P/L) D_h}{(1/2)\rho \overline{u}^2}. \tag{6}$$

The heat transfer rate in the heat exchanger square duct inserted with the 45° ISR is presented with the local Nusselt number and average Nusselt number as follows:

$$\mathrm{Nu}_x = \frac{h_x D_h}{k}, \tag{7}$$

$$\mathrm{Nu} = \frac{1}{L}\int \mathrm{Nu}_x \partial x. \tag{8}$$

The thermal efficiency of the heat exchanger duct equipped with the 45° ISR is presented in the form of thermal enhancement factor or TEF as equation (9). The thermal enhancement factor is defined as the ratio of the heat transfer coefficient of an augmented surface, h, to that of a smooth surface, h_0, at similar pumping power:

$$\mathrm{TEF} = \frac{h}{h_0}\bigg|_{\mathrm{pp}} = \frac{\mathrm{Nu}}{\mathrm{Nu}_0}\bigg|_{\mathrm{pp}} = \frac{\left(\mathrm{Nu}/\mathrm{Nu}_0\right)}{\left(f/f_0\right)^{1/3}}. \tag{9}$$

Nu_0 and f_0 are the Nusselt number and friction factor for the smooth square duct, respectively.

4. Numerical Validation

It is necessary to ensure that the computational domain of the square duct inserted with the 45° ISR has enough reliability to predict flow and heat transfer mechanisms in the tested section. The numerical model of this work is validated. The model validation can be divided into two sections: validation of the smooth duct and grid independence. The verification of the smooth square duct is done by comparing between the present results with the values on both Nusselt number and friction factor from the correlations [29]. The deviations of both values are around ±2% and ±2.5% for the Nusselt number and friction factor, respectively. The verification of the smooth square duct for heat transfer and pressure loss is plotted as Figure 4.

The comparison between five similar models ($b/H = s/H = 0.20$) with different grid cells, 80,000, 120,000, 180,000, 240,000, and 360,000, is done. It is found that the computational domain with the grid around 120,000–360,000 gives similar results for both heat transfer rate and friction loss. Therefore, the grid around 120,000 is applied for all investigated cases of the heat exchanger square duct inserted with the 45° ISR. As the preliminary result, it can be concluded that the numerical model of the heat exchanger square duct inserted with 45° ISR has enough confidentiality to study flow and heat transfer characteristics. The grid independence of the present investigation is reported as Figures 5(a) and 5(b) for Nusselt number ratio and friction factor ratio, respectively.

5. Numerical Result

The numerical result of the heat exchanger square duct inserted with the 45° ISR is separated into two sections: mechanism in the tested duct and performance analysis. The streamlines in transverse planes, temperature distributions

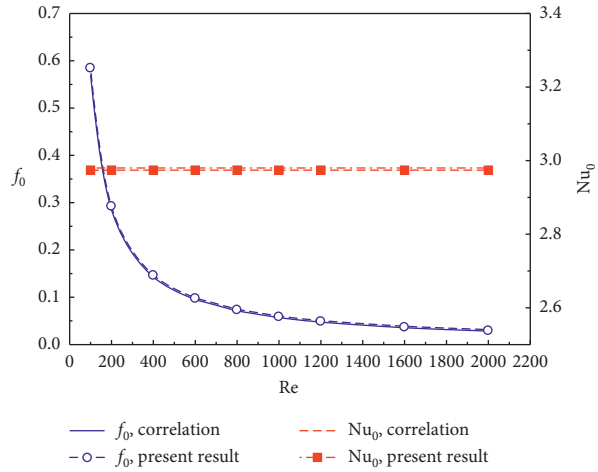

Figure 4: Verification of the smooth square duct.

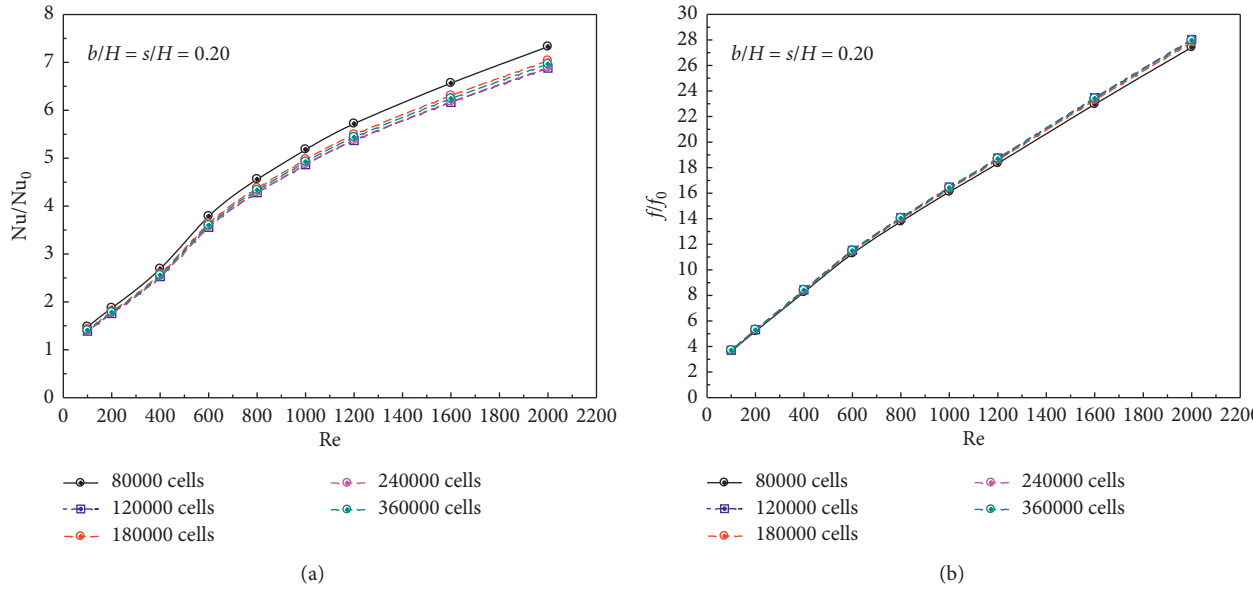

Figure 5: Grid independence for (a) Nusselt number ratio and (b) friction factor ratio.

in transverse planes, and local Nusselt number distributions in the studied section are plotted in the first part of the numerical result. The heat transfer rate, pressure loss, and thermal efficiency of the heating duct installed with the 45° ISR are concluded at the performance analysis part in terms of Nusselt number, friction factor, and thermal enhancement factor, respectively.

5.1. Mechanisms in the Square Duct Equipped with 45° ISR. The streamlines in y-z planes of the heat exchanger square duct installed with the 45° ISR are illustrated as Figures 6(a)–6(g), respectively, for $s/H = 0$, 0.05, 0.10, 0.15, 0.20, 0.25, and 0.30 at $b/H = 0.20$ and Re = 800. The installation of the 45° ISR in the heating section can produce the vortex flow. For $s/H = 0$, the two main vortex flows are found at the upper and lower parts of the plane. When $s/H > 0$, the small vortices near the duct walls are detected. The vortices near the duct wall are found to be larger when enhancing the s/H value. The flow description in the heating duct is presented as Figure 7. The vortex flow in the heating duct will disturb the thermal boundary layer on the duct wall. The thermal boundary layer disturbance in the heating duct is the reason for heat transfer coefficient and performance augmentations. The vortex flow in the tested section also helps for a better air temperature mixing that is another cause for heat transfer and thermal performance increments. The presence of the spacing between the outer edge of the ISR and the duct wall may decrease the strength of the main vortex flow or increase the turbulent fluid mixing.

The thermal boundary layer disturbance in the tested section equipped with the 45° ISR can be considered from the temperature distributions in transverse planes. Figures 8(a)–8(g) report the temperature contours in transverse planes of the heating section installed with the 45° ISR for $s/H = 0$, 0.05, 0.10, 0.15, 0.20, 0.25, and 0.30,

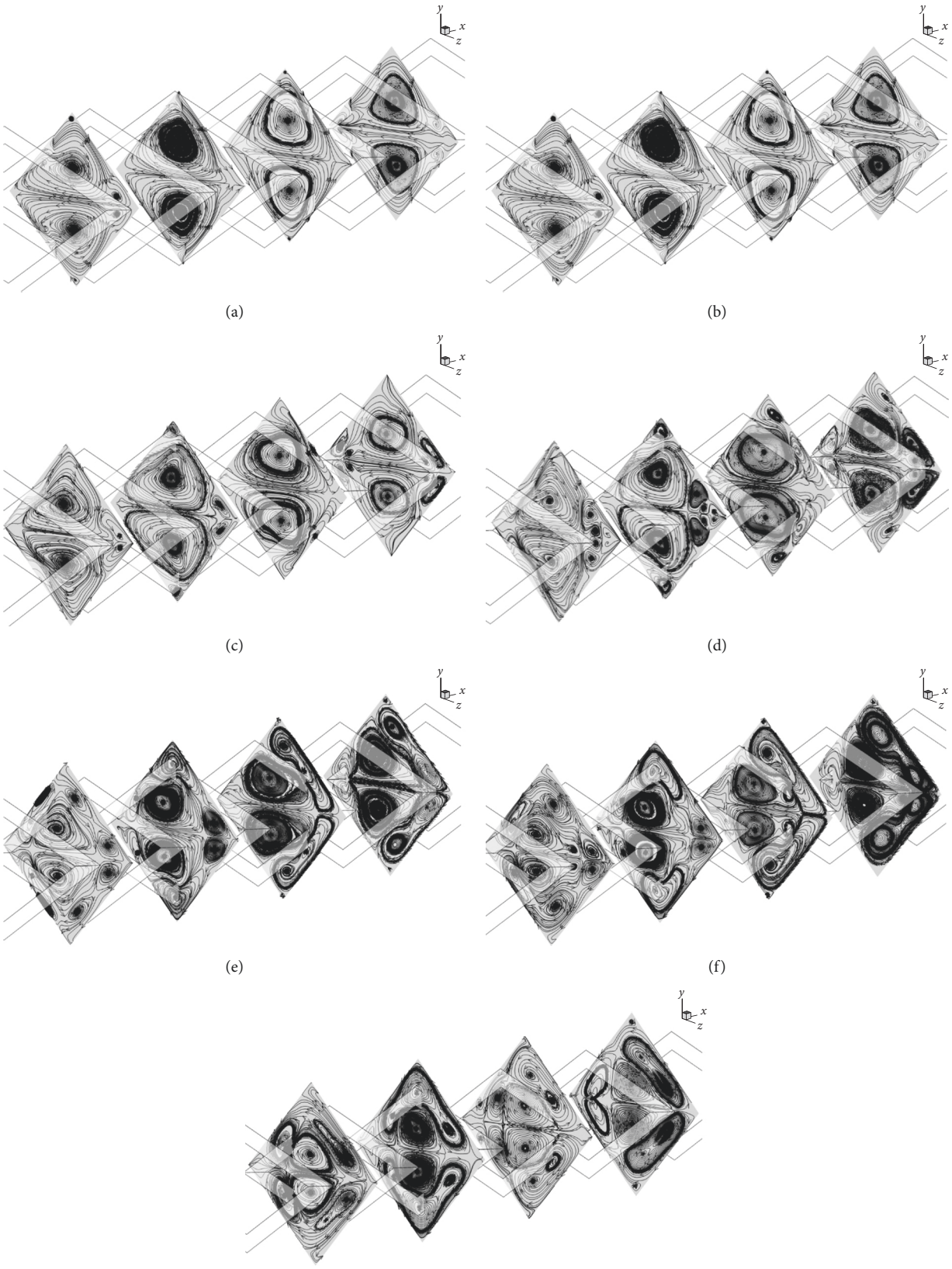

Figure 6: Streamlines in the y-z plane of the heat exchanger square duct installed with the 45° ISR for (a) $s/H = 0$, (b) $s/H = 0.05$, (c) $s/H = 0.10$, (d) $s/H = 0.15$, (e) $s/H = 0.20$, (f) $s/H = 0.25$, and (g) $s/H = 0.30$ at BR = 0.20 and Re = 800.

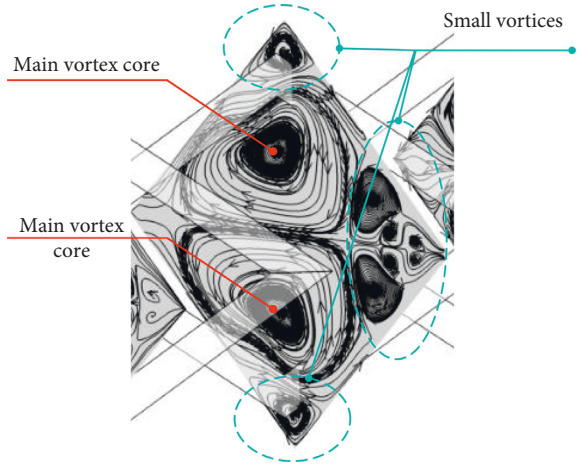

Figure 7: Flow description.

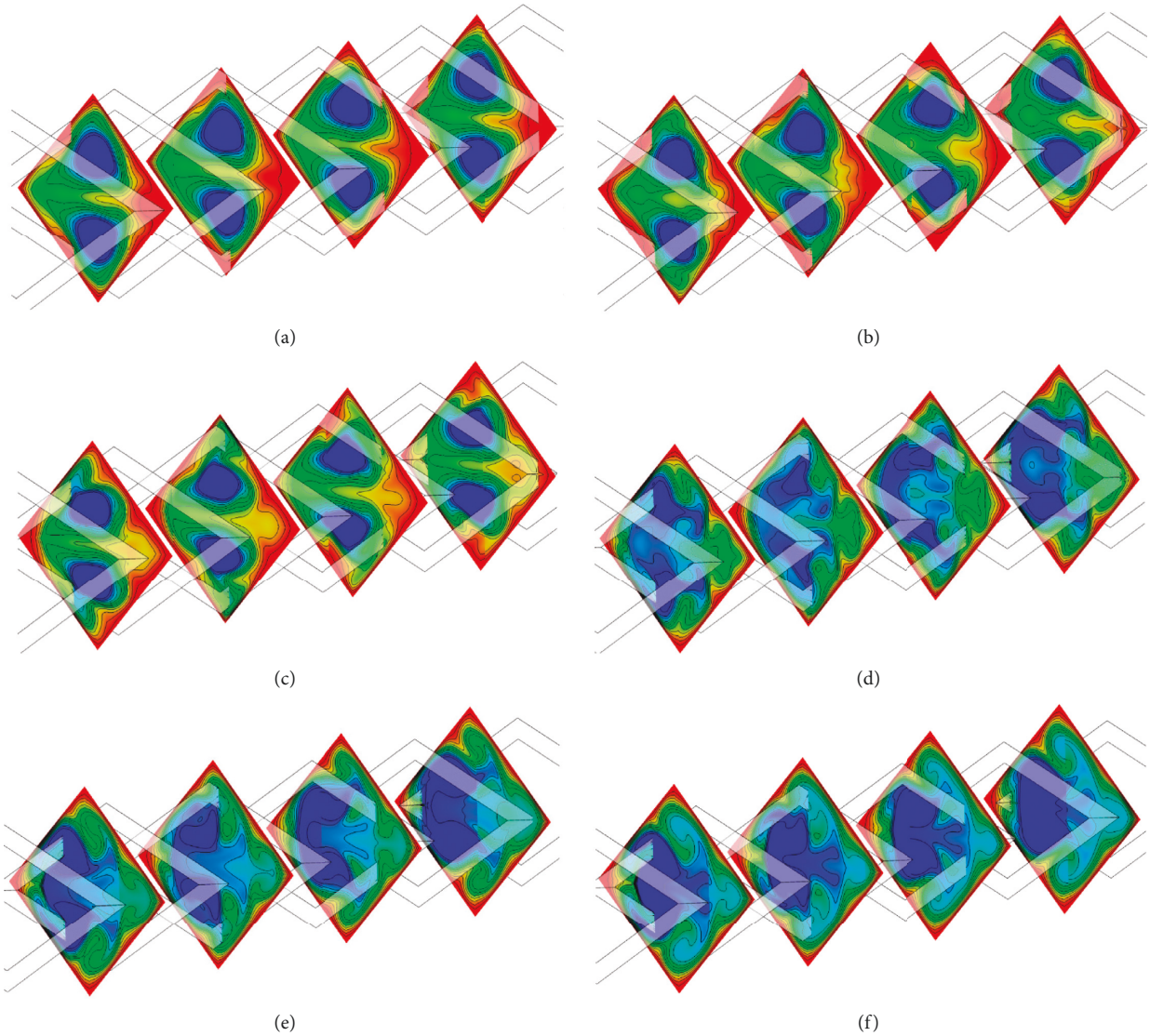

Figure 8: Continued.

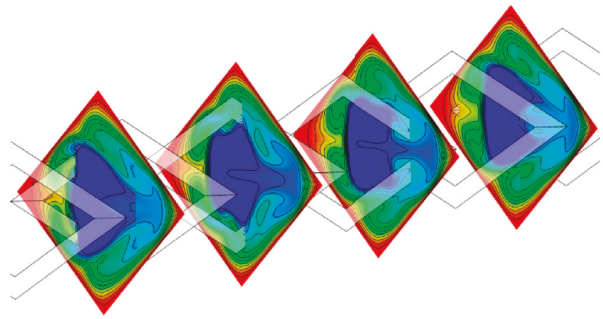

(g)

Figure 8: Temperature contours in the y-z plane of the heat exchanger square duct installed with the 45° ISR for (a) $s/H = 0$, (b) $s/H = 0.05$, (c) $s/H = 0.10$, (d) $s/H = 0.15$, (e) $s/H = 0.20$, (f) $s/H = 0.25$, and (g) $s/H = 0.30$ at BR = 0.20 and Re = 800.

respectively, at Re = 800 and $b/H = 0.20$. In general, the blue contour (low-temperature air) is found at the center of the square duct, while the red contour (high-temperature fluid) is detected near the duct walls for the smooth duct with no ISR. The vortex flow, which is created by the 45° ISR in the heating system, can disturb the thermal boundary layer in all cases. As shown in figures, the blue layer distributes from the center of the plane, while the red layer is found to decrease when compared with the smooth duct. The thickness of the red layer near the duct walls extremely decreases when $s/H > 0.10$. The configuration of the heat transfer is not similar when the s/H value is changed. The s/H value around 0.15–0.30 gives the better fluid mixing than the s/H value around 0–0.10.

The local Nusselt number distributions on the duct walls of the heat exchanger square duct inserted with the 45° ISR are plotted as Figures 9–14, respectively, at Re = 800 of $b/H = 0.05$, 0.10, 0.15, 0.20, 0.25, and 0.30. The wall code for the heat exchanger square duct inserted with the 45° ISR is printed as Figure 15. For $b/H = 0.05$, $s/H = 0.05$ provides the highest heat transfer rate at wall_A and wall_B. The local Nusselt number at wall_A and wall_B decreases when increasing s/H value, but the local Nusselt number at wall_C and wall_D performs the reverse trend.

Seeing at $b/H = 0.10$, the local Nusselt number at wall_C and wall_D enhances when augmenting s/H. $s/H = 0$ shows the highest heat transfer rate at wall_A and wall_B. The lowest heat transfer rate at wall_A and wall_B is found at $s/H = 0.05$.

Considering at $b/H = 0.15$, Nu_x at wall_C and wall_D enhances when increasing s/H. At wall_A and wall_B, $s/H = 0.30$ gives the highest heat transfer rate, while $s/H = 0$ performs the opposite result. The peak of the local Nusselt number at wall_A and wall_B is found at $s/H = 0.15$–0.25.

For $b/H = 0.20$ at wall_A and wall_B, the maximum value of the local Nusselt number is found at $s/H = 0.15$–0.20. The peak of heat transfer rate at wall_C and wall_D is detected at $s/H = 0.20$–0.30.

At $b/H = 0.25$, the highest heat transfer rate at wall_A and wall_B is found at $s/H = 0.10$–0.15. For all duct walls, the local Nusselt number enhances when $0 \le s/H \le 0.15$ but decreases when $s/H > 0.15$.

For $b/H = 0.30$, the maximum value of heat transfer rate at wall_A and wall_B appears at $s/H = 0.10$. Considering all sidewalls of the duct, the local Nusselt number develops when $0 \le s/H \le 0.15$ but drops when $s/H > 0.15$.

Considering a similar s/H value, the augmentation on b/H of the 45° ISR brings very close structure in both heat transfer and flow behaviors in the heat exchanger duct.

5.2. Performance Analysis. The Nusselt number ratio is plotted with the Reynolds number at various s/H values for $b/H = 0.05$, 0.10, 0.15, 0.20, 0.25, and 0.30 as Figures 16(a)–16(f), respectively. The heat exchanger square duct inserted with the 45° ISR brings higher heat transfer rate than the smooth duct in all investigated cases. Nu/Nu_0 is greater than the unity. In most cases, the Nusselt number enhances when augmenting the Reynolds number. In the range investigated, the average Nusselt number is around 1.02–2.46, 1.02–4.44, 1.03–5.68, 1.15–7.27, 1.36–10.05, and 1.54–9.30 times over the smooth square duct for $b/H = 0.05$, 0.10, 0.15, 0.20, 0.25, and 0.30, respectively.

The relation of the friction factor ratio with the Reynolds number for the heating duct installed with the 45° ISR is plotted as Figures 17(a)–17(f), respectively, for b/H = 0.05, 0.10, 0.15, 0.20, 0.25, and 0.30. The attachment of the 45° ISR in the heat exchanger square channel provides higher friction loss than the smooth duct with no ISR. The friction factor increases when increasing the Reynolds number. The extreme increment of the friction loss is found at high b/H and Re values. $s/H = 0$ provides the lowest friction loss in all b/H values.

Seeing at $b/H = 0.05$ and $0 \le s/H \le 0.25$, f/f_0 enhances when augmenting s/H values. f/f_0 of $s/H = 0.25$ and 0.30 is found to be very close. $b/H = 0.05$ performs the friction loss around 1–3.92 times above the smooth duct for $s/H = 0$–0.30 and Re = 100–2000.

For $0 \le s/H \le 0.25$, the pressure loss in the tested section augments when enhancing s/H at $b/H = 0.10$. $s/H = 0.30$ gives lower friction loss than $s/H = 0.25$ when Re > 600. In the range studies, $b/H = 0.10$ performs the pressure loss higher than the base case around 1–9.52 times depending on Re and s/H values.

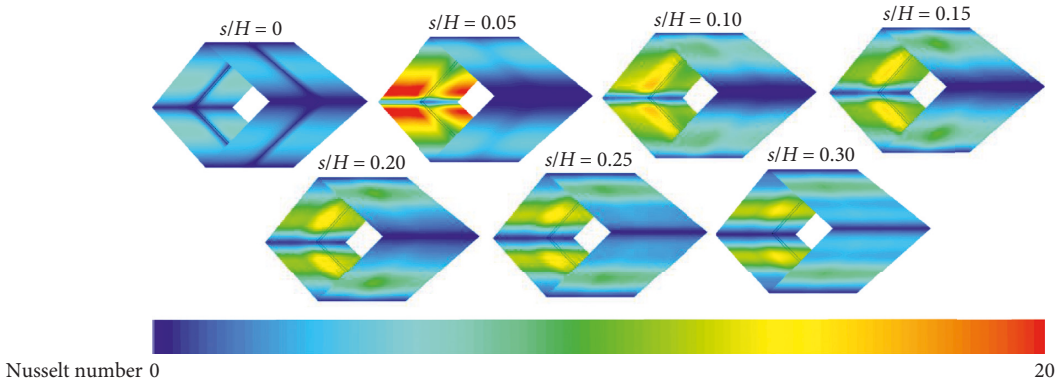

Figure 9: Nu_x of the heat exchanger square duct installed with the 45° ISR for BR = 0.05 and Re = 800.

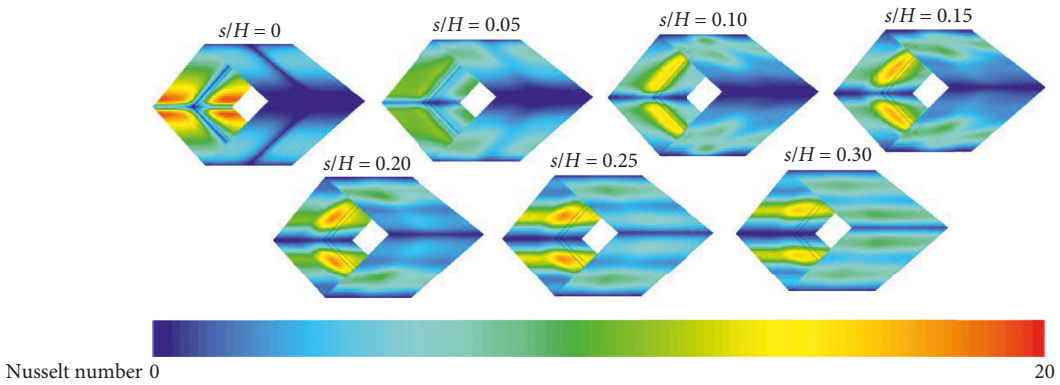

Figure 10: Nu_x of the heat exchanger square duct installed with the 45° ISR for BR = 0.10 and Re = 800.

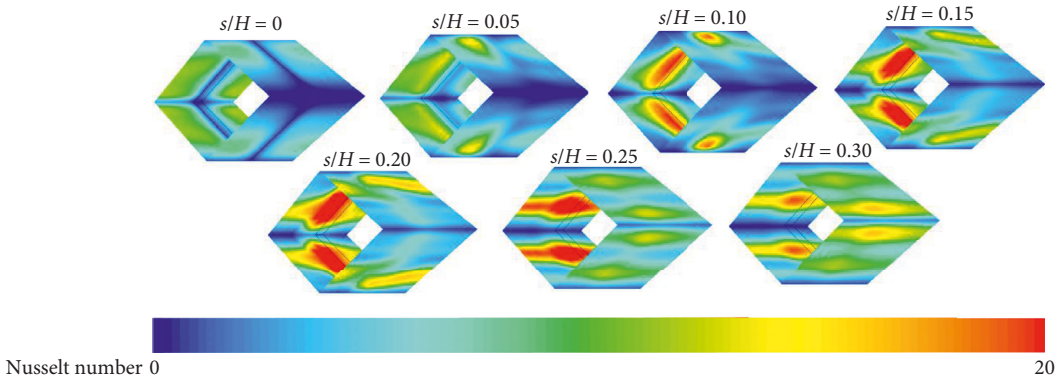

Figure 11: Nu_x of the heat exchanger square duct installed with the 45° ISR for BR = 0.15 and Re = 800.

At $b/H = 0.15$ and 0.20, $0 \le s/H \le 0.20$, the friction loss increases when improving the s/H value. f/f_0 is found to be around 1.13–17.15 and 1.47–28.03 times over the smooth duct, respectively, for $b/H = 0.15$ and 0.20.

In the range $0 \le s/H \le 0.10$ at $b/H = 0.25$, the pressure loss augments when inducing the s/H value. The 45° ISR with $b/H = 0.25$ brings the greater pressure loss around 2.15–45.83 times than the smooth duct.

When increasing s/H, the pressure drop in the tested section with the 45° ISR at $b/H = 0.30$ reduces. f/f_0 in the studied section is about 3.40–64.79 when inserting $b/H = 0.30$ of the 45° ISR.

The variation of the TEF with the Reynolds number at various cases is presented as Figures 18(a)–18(f), respectively, for the heating duct equipped with the 45° ISR at $b/H = 0.05$, 0.10, 0.15, 0.20, 0.25, and 0.30. The presence of the

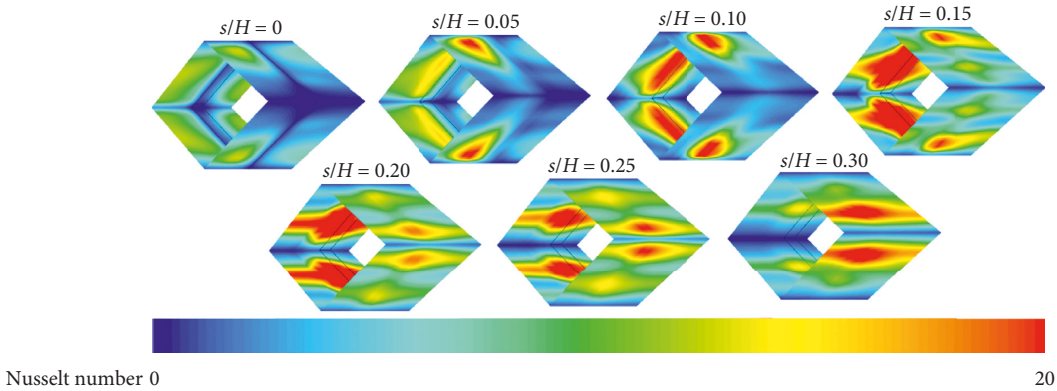

Figure 12: Nu_x of the heat exchanger square duct installed with the 45° ISR for BR = 0.20 and Re = 800.

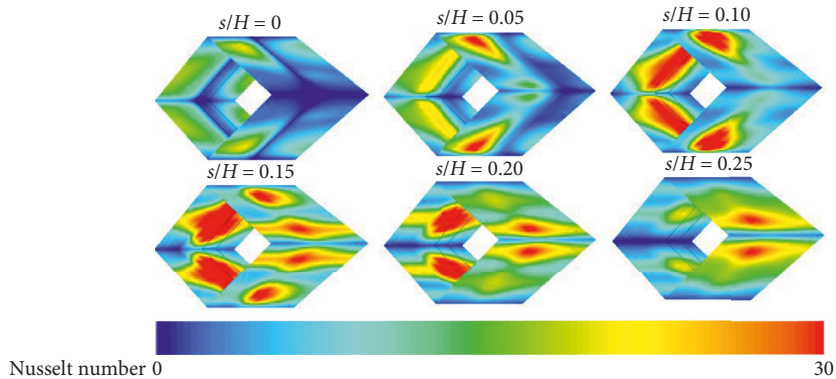

Figure 13: Nu_x of the heat exchanger square duct installed with the 45° ISR for BR = 0.25 and Re = 800.

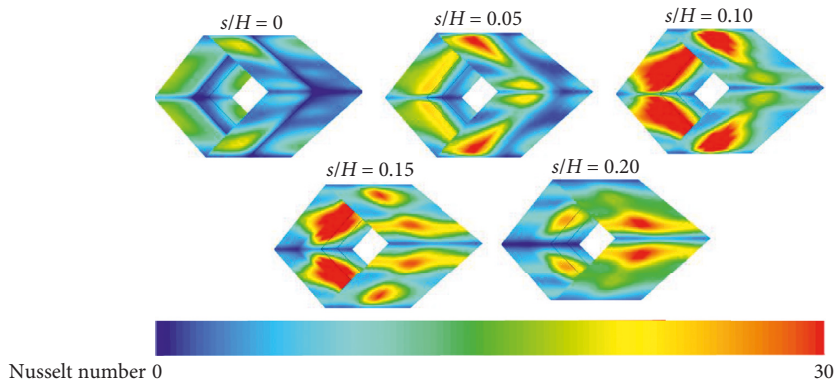

Figure 14: Nu_x of the heat exchanger square duct installed with the 45° ISR for BR = 0.30 and Re = 800.

45° ISR in the heat exchanger duct performs higher TEF than the smooth duct with no ISR (TEF > 1) in almost cases. The maximum TEF in the range investigated is around 1.94, 2.11, 2.23, 2.45, 2.84, and 2.52 for the heating section with the 45° ISR at b/H = 0.05, 0.10, 0.15, 0.20, 0.25, and 0.30, respectively.

The relation of Nu/Nu_0, $f/f_{0,}$ and TEF with s/H for the heat exchanger duct at various b/H and Re values is shown as Figures 19–21, respectively. Considering Re = 2000, the peak of heat transfer rate is detected at s/H = 0.05, 0.30, 0.25, 0.15, 0.10, and 0.10 for the 45° ISR with b/H = 0.05, 0.10, 0.15, 0.20, 0.25, and 0.30, respectively. The insertion of the 45° ISR in the studied section not only improves heat transfer rate but also enhances pressure loss. The maximum pressure loss in the tested section is found at s = 30, 25, 20, 20, 15, and 15% of the duct height, respectively, for b/H = 0.05, 0.10, 0.15, 0.20, 0.25, and 0.30 when considering Re = 2000. Because the installation of the 45° ISR in the tested duct brings greater heat transfer rate and pressure loss than the smooth duct, the TEF is selected to analyze the efficiency of the present tested section. The greatest TEF is detected at s/H around 0.05, 0.30,

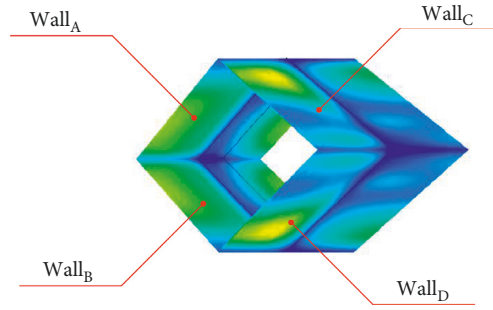

Figure 15: Wall code.

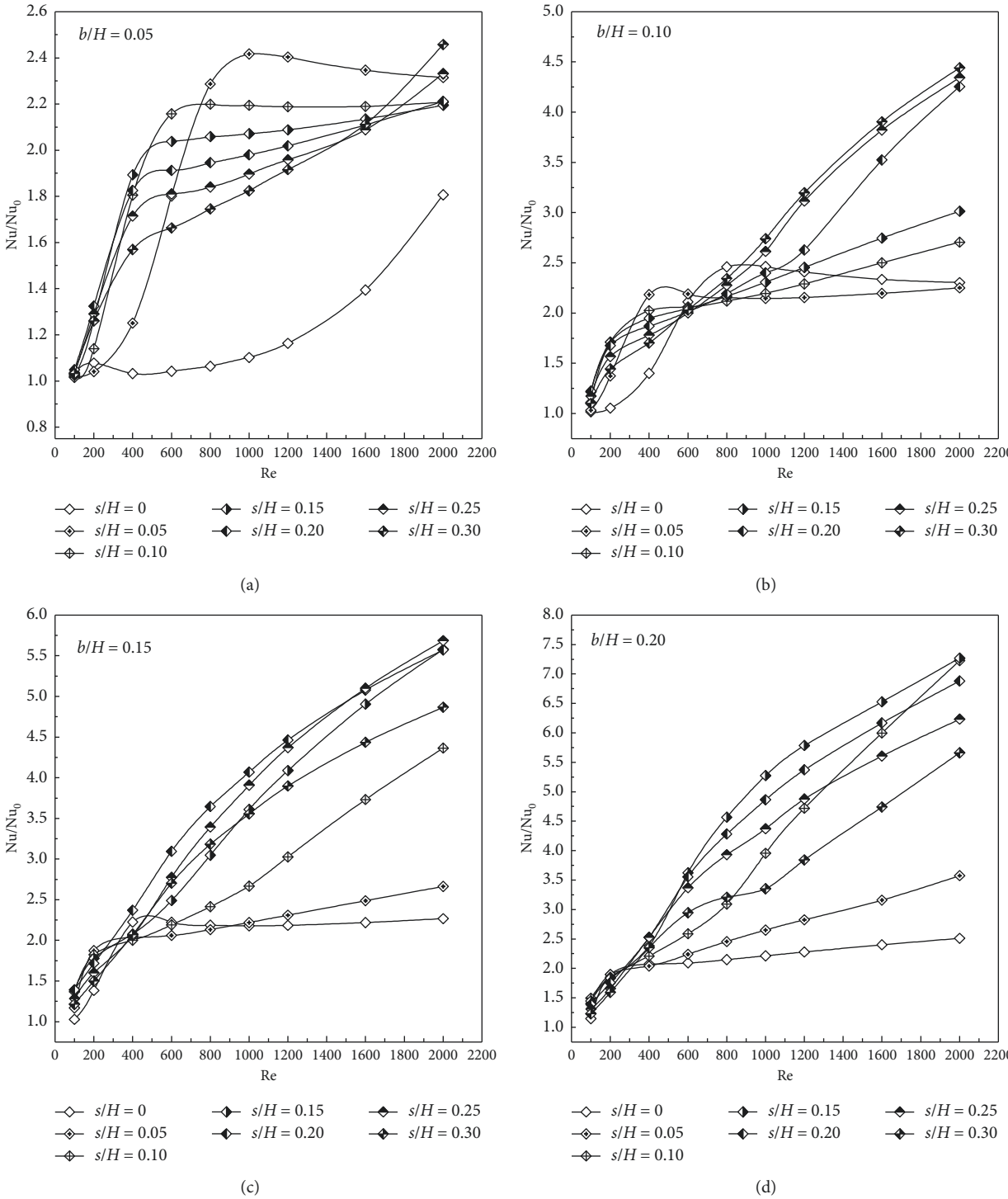

Figure 16: Continued.

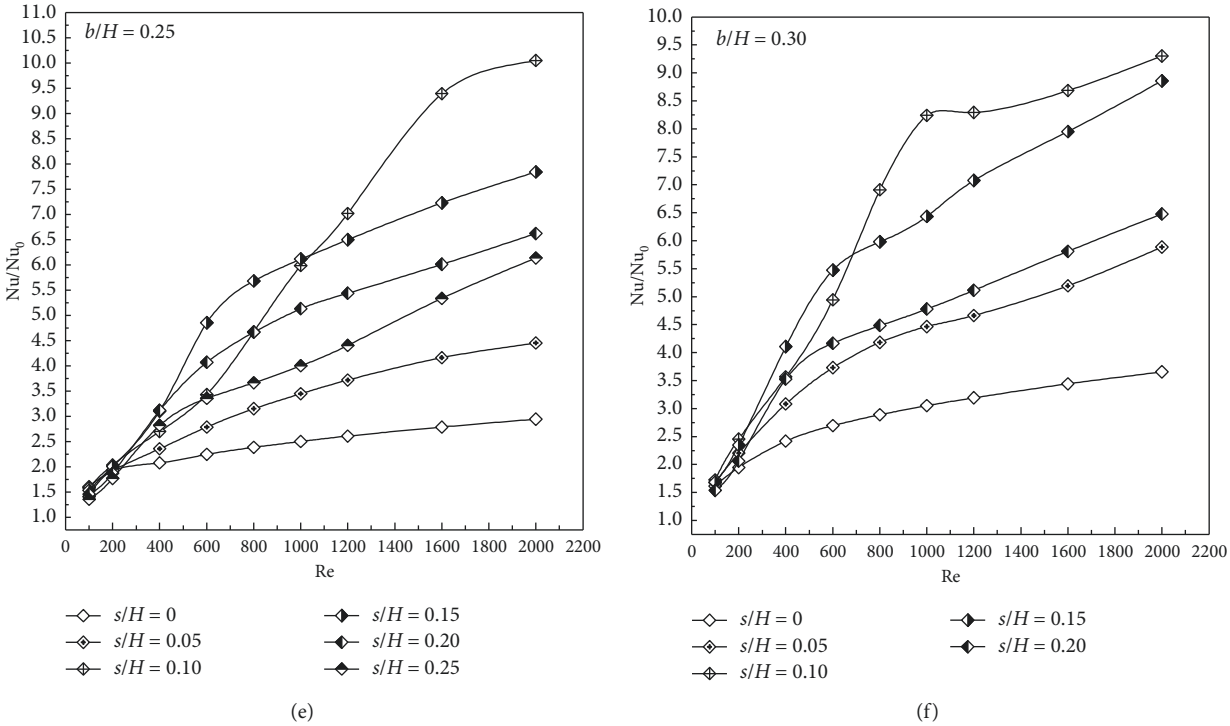

Figure 16: Nu/Nu_0 versus Reynolds number for the heat exchanger square duct installed with the 45° ISR at (a) $b/H = 0.05$, (b) $b/H = 0.10$, (c) $b/H = 0.15$, (d) $b/H = 0.20$, (e) $b/H = 0.25$, and (f) $b/H = 0.30$.

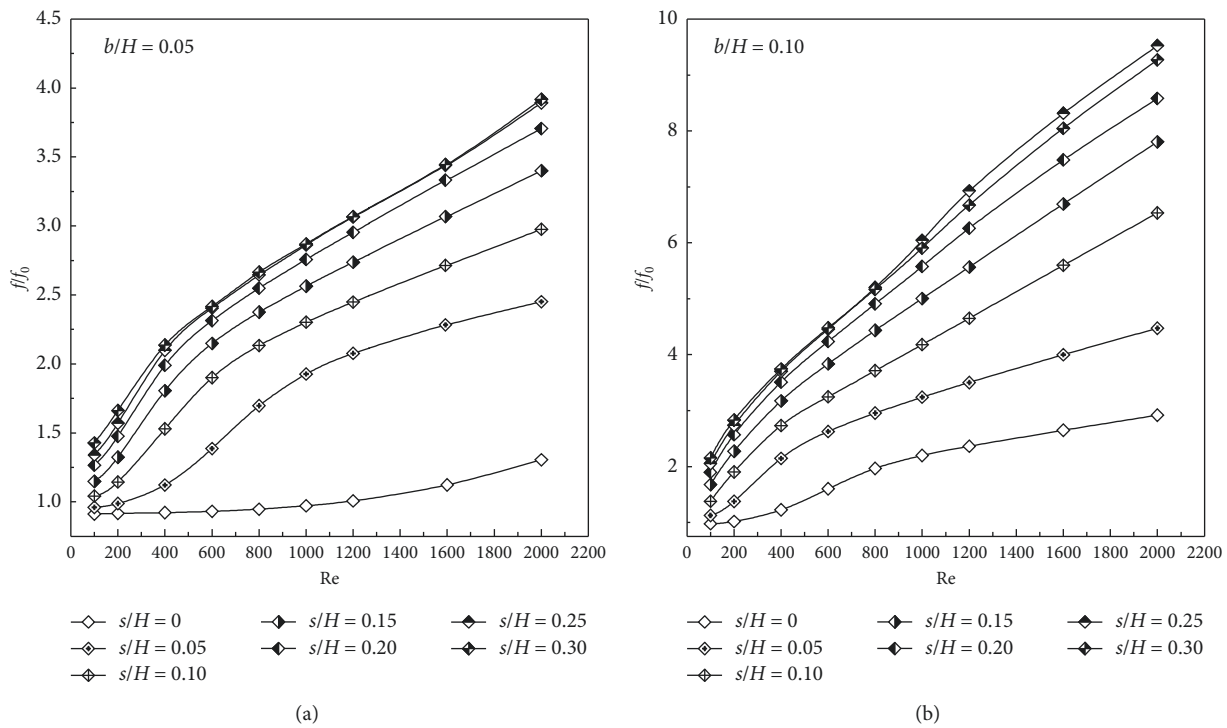

Figure 17: Continued.

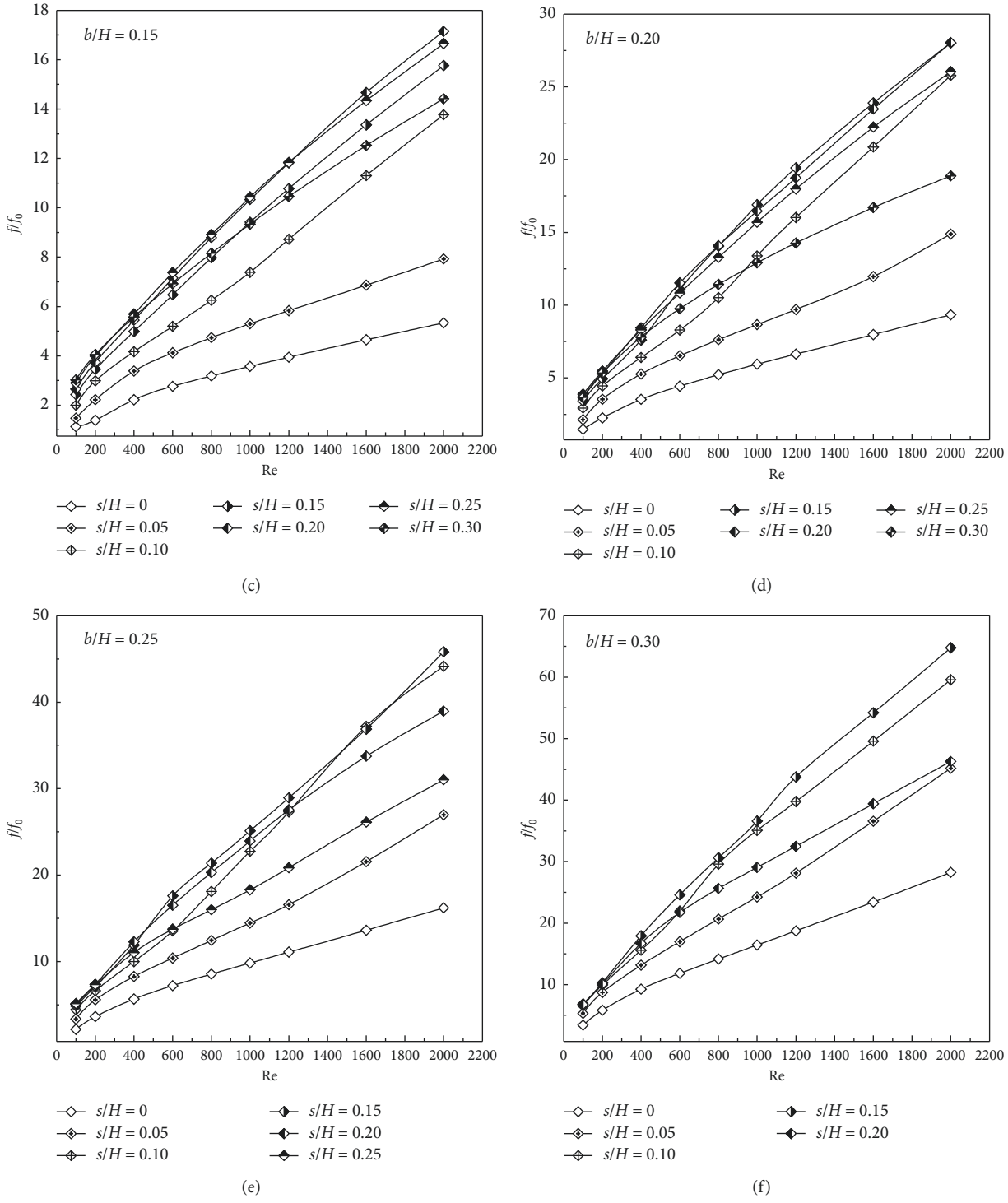

FIGURE 17: f/f_0 versus Reynolds number for the heat exchanger square duct installed with the 45° ISR at (a) $b/H = 0.05$, (b) $b/H = 0.10$, (c) $b/H = 0.15$, (d) $b/H = 0.20$, (e) $b/H = 0.25$, and (f) $b/H = 0.30$.

0.15, 0.10, 0.10, and 0.10, respectively, for the square duct with the 45° ISR at b/H around 0.05, 0.10, 0.15, 0.20, 0.25, and 0.30.

Figures 22(a) and 22(b) present the average Nu/Nu_0 versus b/H and average f/f_0 versus b/H in the heat exchanger duct inserted with the 45° ISR, respectively. The average Nusselt number in the heat exchanger square duct inserted with the 45° ISR increases when augmenting the b/H value, except for $s/H = 0.20$ and 0.25. The average Nusselt number ratio in the heat exchanger square duct inserted with the 45° ISR slightly decreases when $b/H > 0.25$ and 0.20 for $s/H = 0.20$ and 0.25, respectively. For $s/H = 0$, the 45° ISR gives

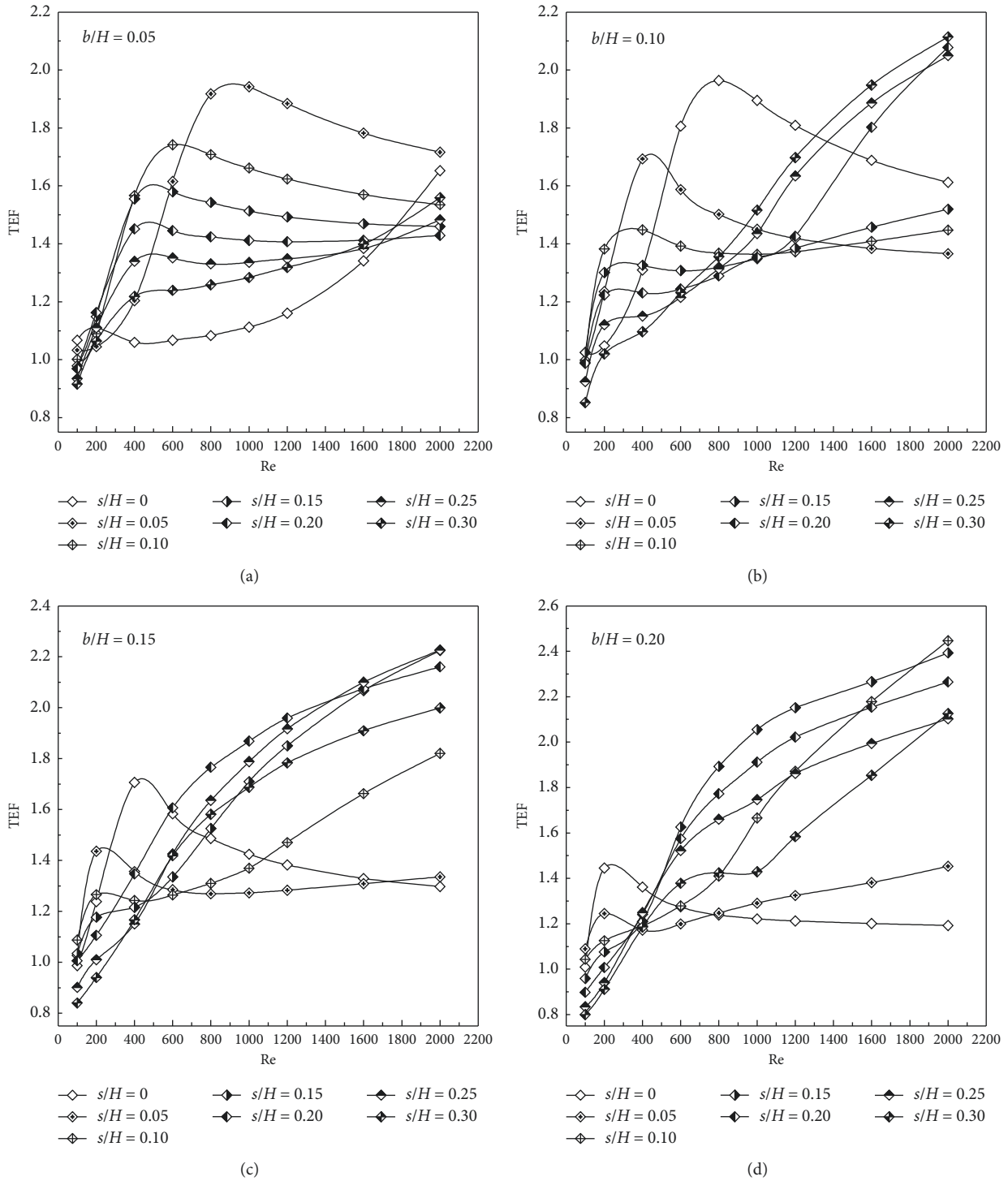

Figure 18: Continued.

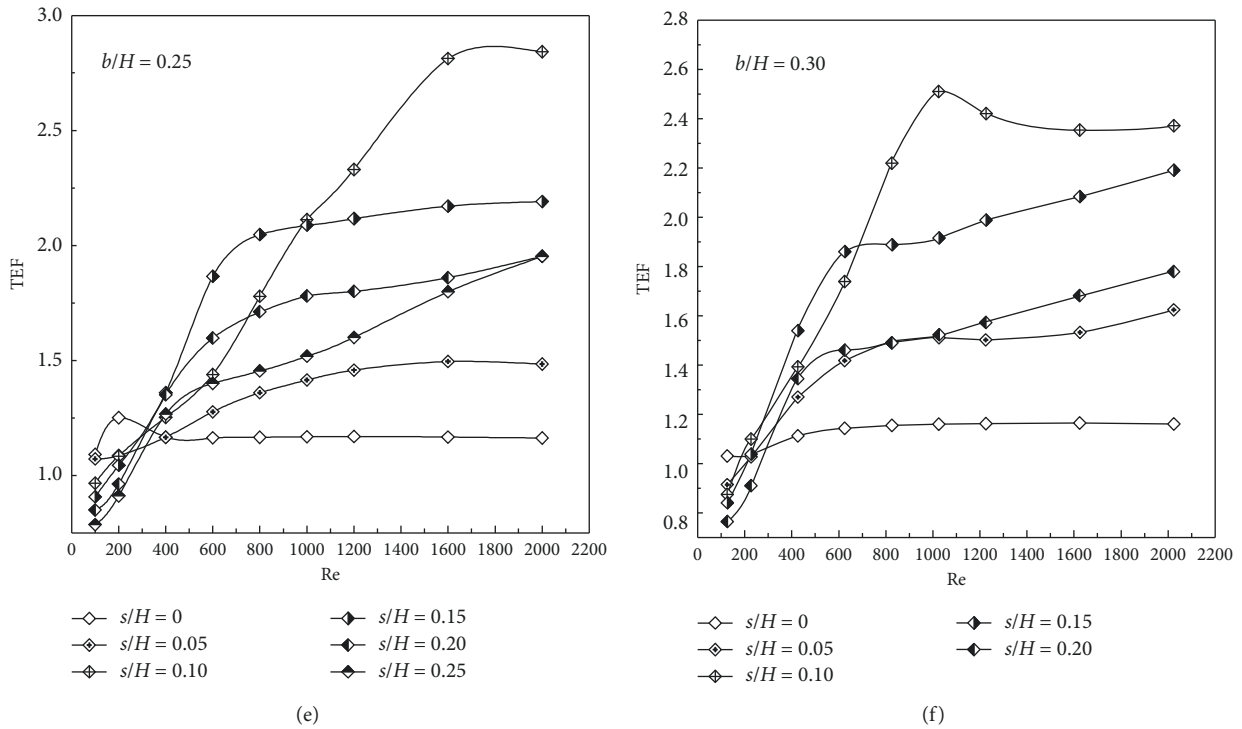

Figure 18: TEF versus Reynolds number for the heat exchanger square duct installed with the 45° ISR at (a) $b/H = 0.05$, (b) $b/H = 0.10$, (c) $b/H = 0.15$, (d) $b/H = 0.20$, (e) $b/H = 0.25$, and (f) $b/H = 0.30$.

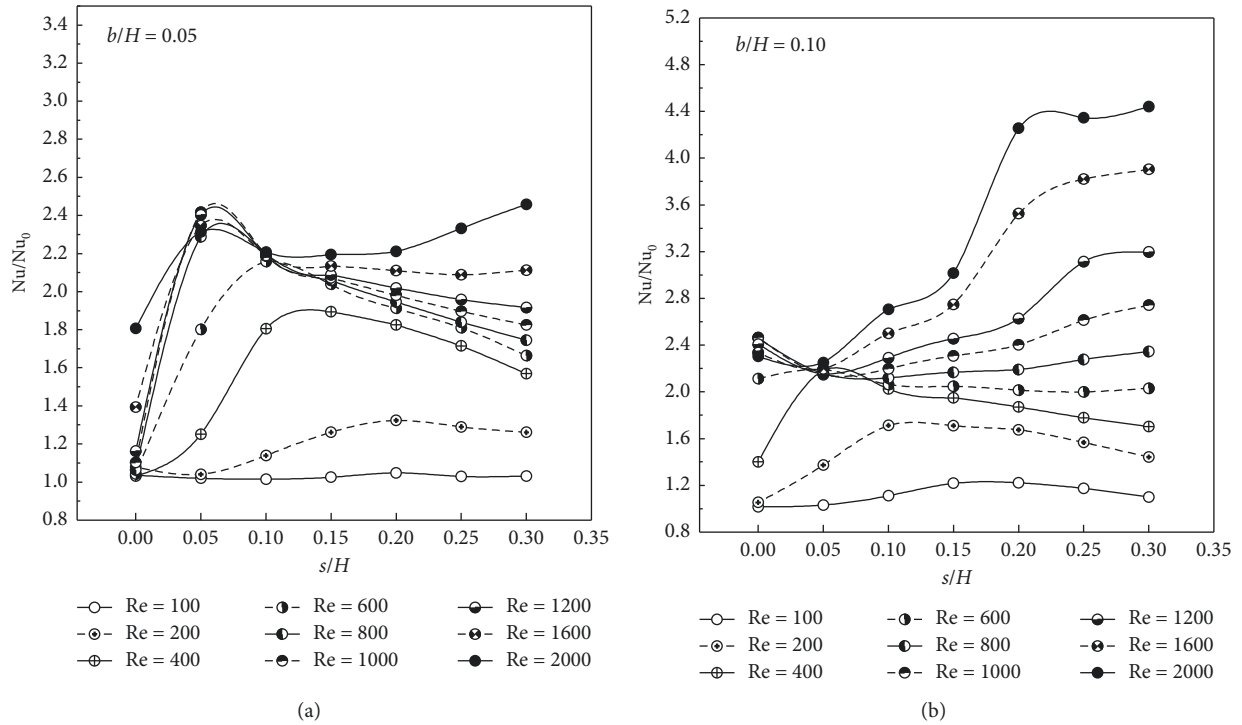

Figure 19: Continued.

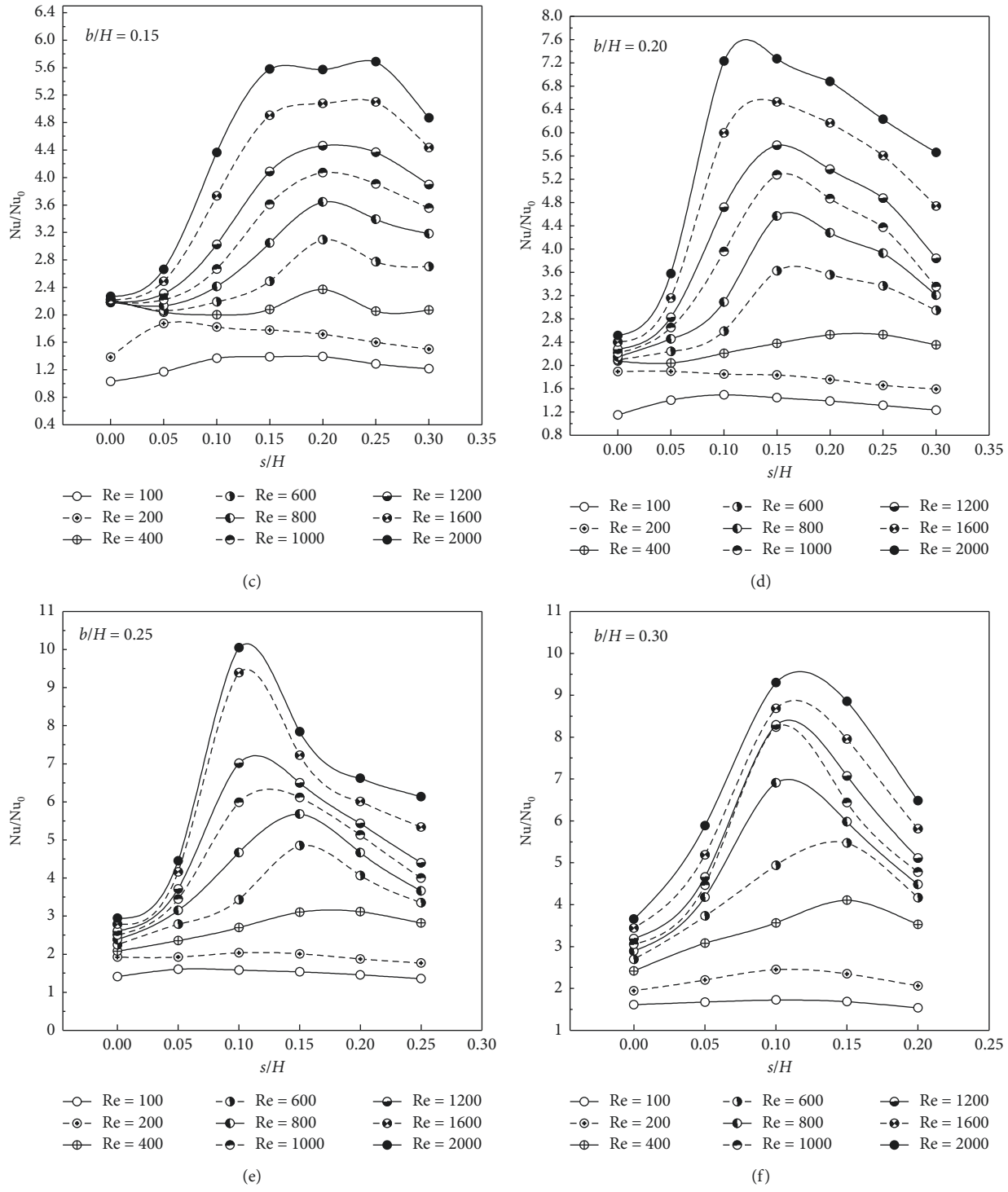

FIGURE 19: Nu/Nu_0 versus s/H for the heat exchanger square duct installed with the 45° ISR at (a) $b/H = 0.05$, (b) $b/H = 0.10$, (c) $b/H = 0.15$, (d) $b/H = 0.20$, (e) $b/H = 0.25$, and (f) $b/H = 0.30$.

the average Nu/Nu_0 around 1.19, 1.95, 1.99, 2.08, 2.32, and 2.77, respectively, for $b/H = 0.05$, 0.10, 0.15, 0.20, 0.25, and 0.30. At $s/H = 0.05$, the average Nusselt number is around 1.88, 1.96, 2.11, 2.47, 3.07, and 3.90 greater than the smooth duct for $b/H = 0.05$, 0.10, 0.15, 0.20, 0.25, and 0.30, respectively. The average Nu/Nu_0 is around 1.90, 2.08, 2.62, 3.68, 5.21, and 6.01, respectively, for $b/H = 0.05$, 0.10, 0.15, 0.20, 0.25, and 0.30 at $s/H = 0.10$. For $s/H = 0.15$, the average Nu/Nu_0 is around 1.86, 2.18, 3.22, 4.30, 4.98, and 5.55, respectively, for $b/H = 0.05$, 0.10, 0.15, 0.20, 0.25, and 0.30. The average Nu/Nu_0 is found to be around 1.82, 2.42, 3.49, 4.09, 4.26, and 4.22 for $b/H = 0.05$, 0.10, 0.15, 0.20, 0.25, and

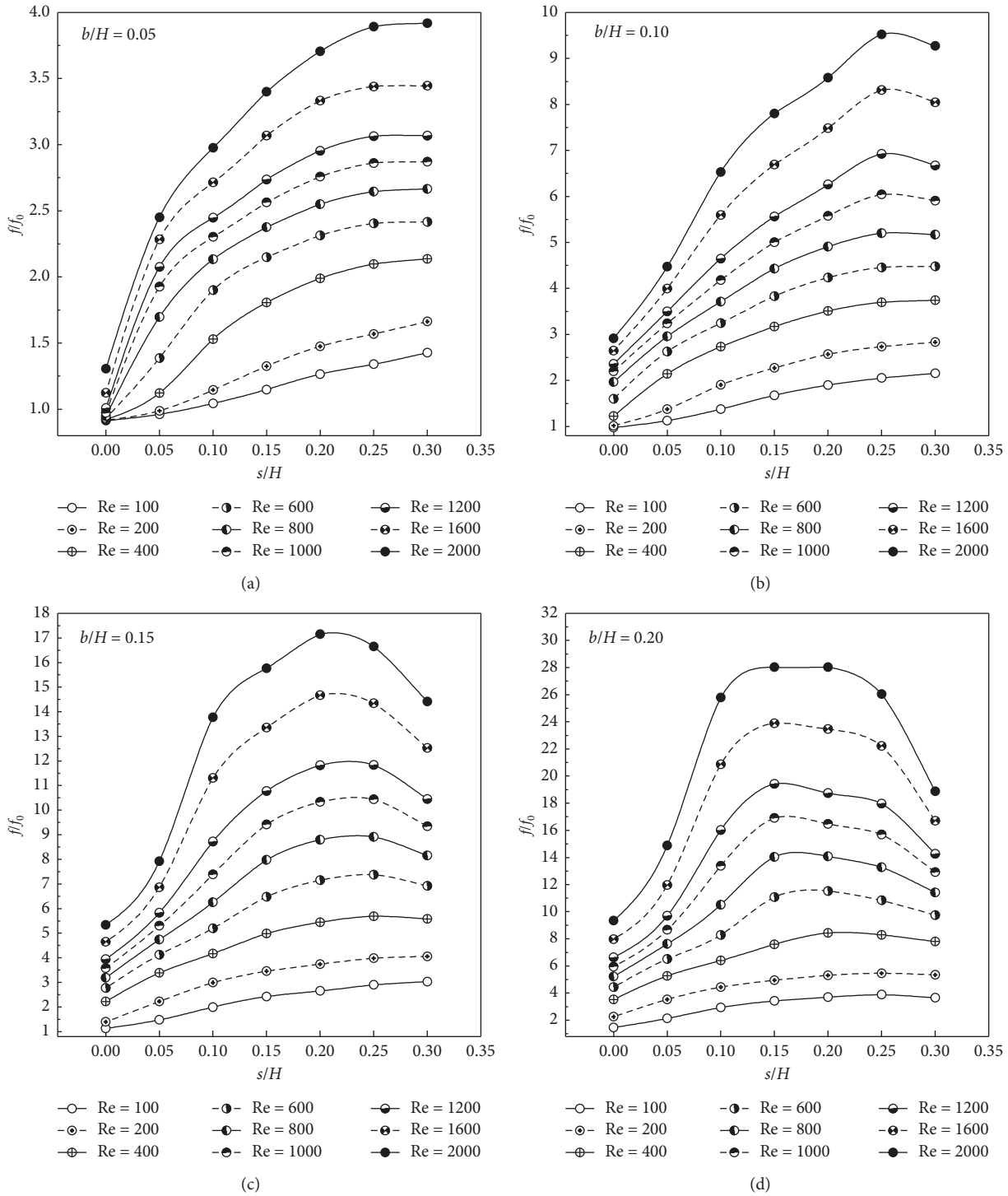

Figure 20: Continued.

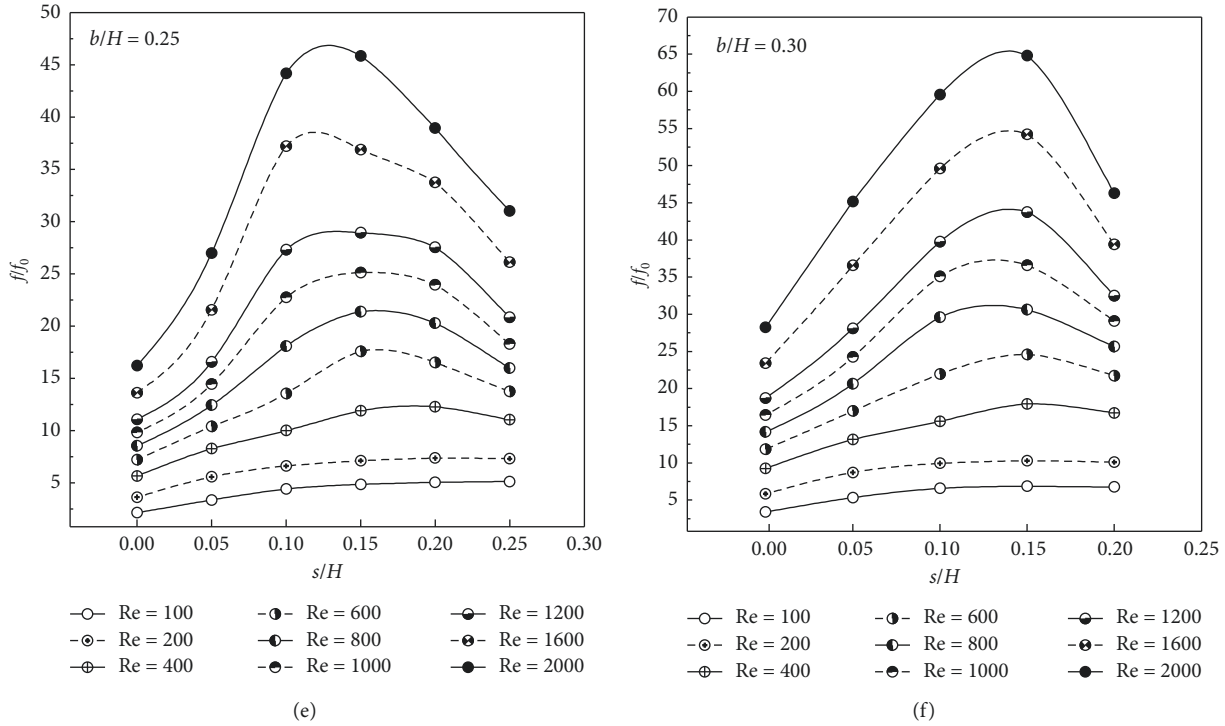

FIGURE 20: f/f_0 versus s/H for the heat exchanger square duct installed with the 45° ISR at (a) $b/H = 0.05$, (b) $b/H = 0.10$, (c) $b/H = 0.15$, (d) $b/H = 0.20$, (e) $b/H = 0.25$, and (f) $b/H = 0.30$.

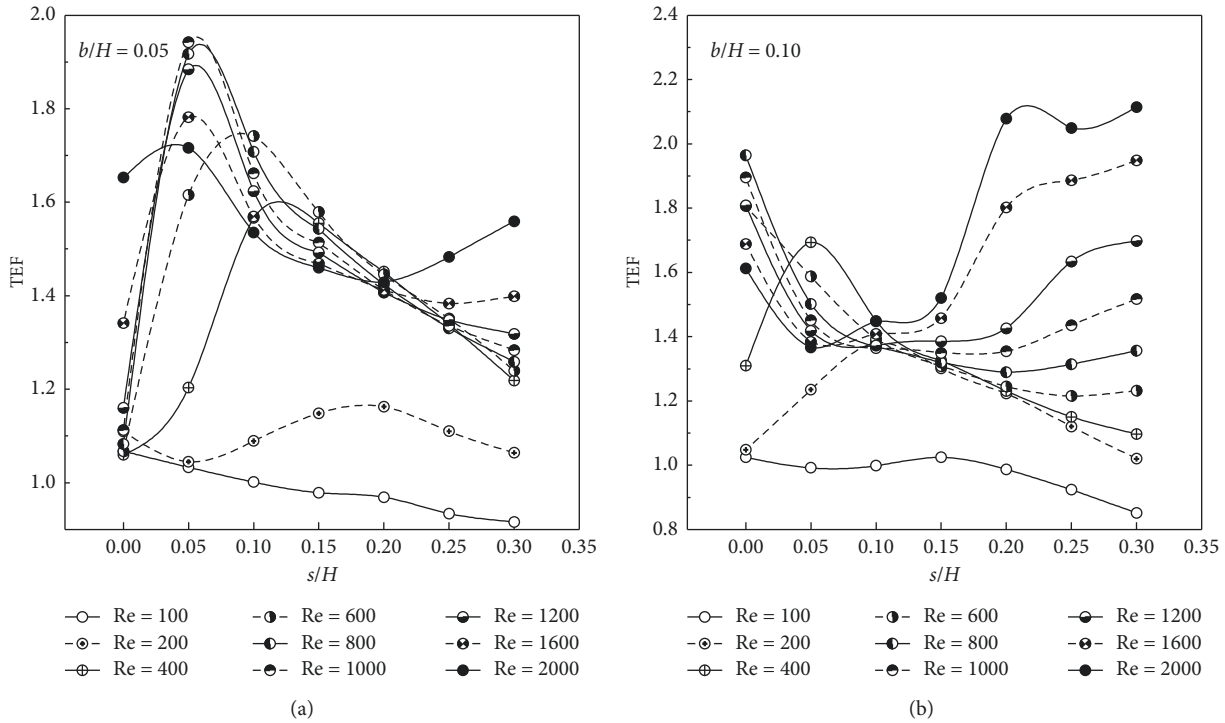

FIGURE 21: Continued.

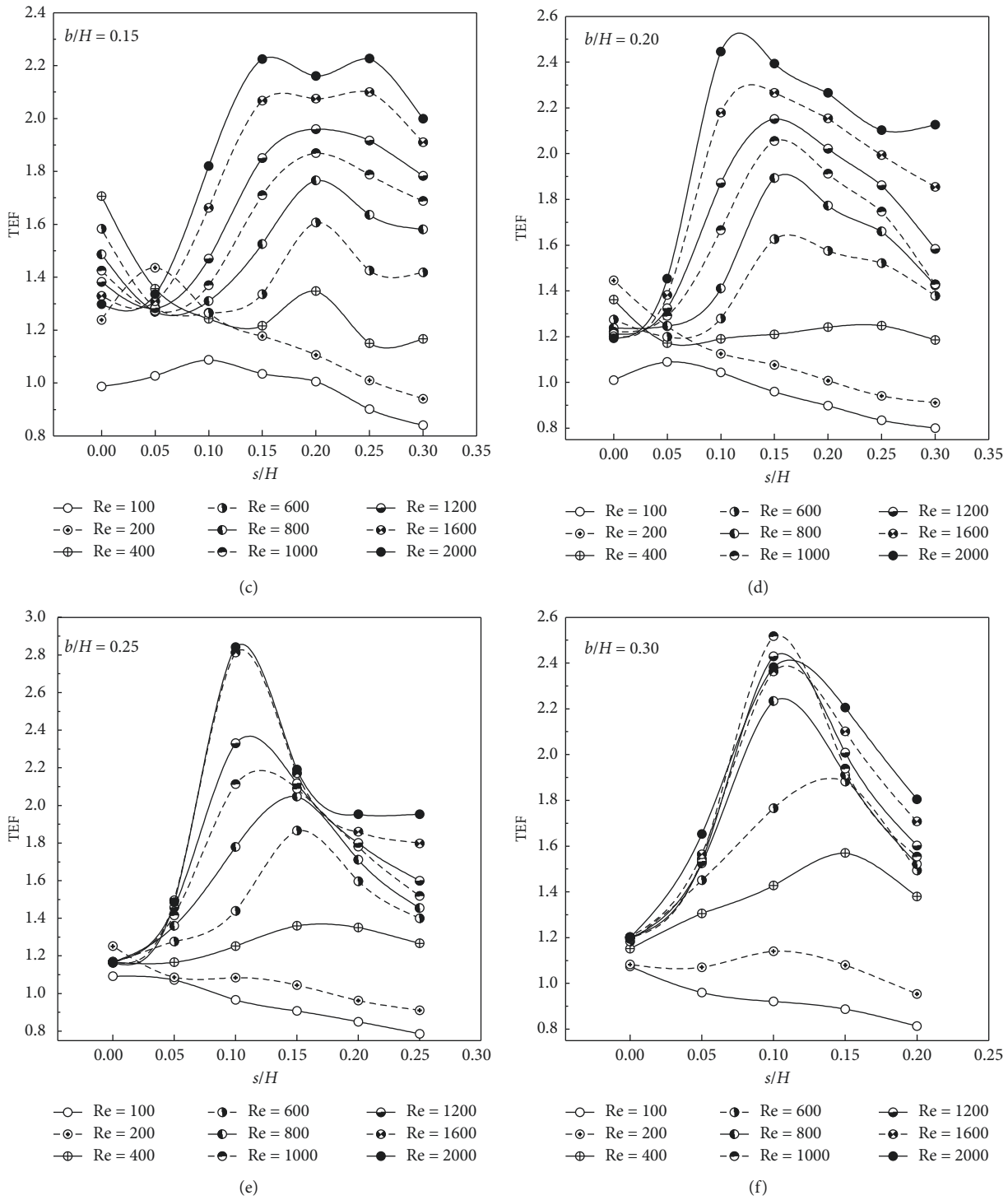

FIGURE 21: TEF versus s/H for the heat exchanger square duct installed with the 45° ISR at (a) $b/H = 0.05$, (b) $b/H = 0.10$, (c) $b/H = 0.15$, (d) $b/H = 0.20$, (e) $b/H = 0.25$, and (f) $b/H = 0.30$.

0.30, respectively, at $s/H = 0.20$. The 45° ISR with $s/H = 0.25$ provides the average Nu/Nu_0 around 1.77, 2.52, 3.35, 3.75, and 3.65 for $b/H = 0.05$, 0.10, 0.15, 0.20, and 0.25, respectively. At $s/H = 0.30$, Nu/Nu_0 is around 1.73, 2.54, 3.05, and 3.21, respectively, for $b/H = 0.05$, 0.10, 0.15, and 0.20. The average f/f_0 augments when enhancing b/H for all s/H values. In the range studies, f/f_0 in the heat exchanger duct fitted with the 45° ISR is around 1.00–28.25, 1.00–45.18,

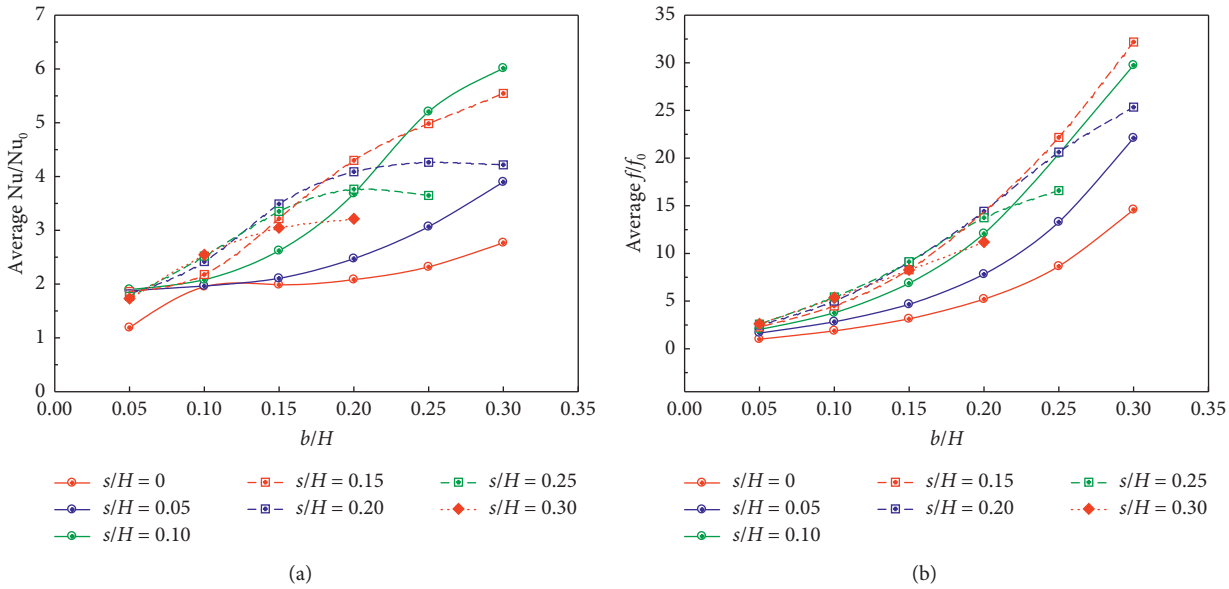

FIGURE 22: (a) Average Nu/Nu_0 vs b/H and (b) average f/f_0 vs b/H for the heat exchanger square duct installed with the 45° ISR at various s/H values.

1.04–59.57, 1.15–64.79, 1.27–46.29, 1.34–31.02, and 1.42–18.89, respectively, for $s/H = 0$, 0.05, 0.10, 0.15, 0.20, 0.25, and 0.30.

6. Conclusion

Numerical analysis on flow topology and heat transfer behavior in the heat exchanger duct installed with 45° ISR is reported. The influences on flow and heat transfer mechanisms for the ISR size and placement in the square duct are considered for laminar flow regime with the Reynolds number around 100–2000. The conclusions for the present investigation are as follows.

The installation of the 45° ISR in the tested section brings higher pressure drop and heat transfer rate than the general square duct for all tested cases. In the range studies, the Nusselt number and friction factor are around 1.00–10.05 and 1.00–64.79 times over the general square duct with no ISR, respectively. The optimum thermal enhancement factor for the present work is around 2.84 at $b/H = 0.25$ and $s/H = 0.10$.

The ISR size and placement effect changes both flow and heat transfer structures in the square duct. The difference of the s/H and b/H values changes the impinging position of the vortex flow on the duct walls and also reduces or increases the strength of the vortex flow. For the present research, the suggestion for the spacing between the outer edge of the ISR and the duct wall is around $0.10H$ with the recommendation of the ring height around $0.20–0.30H$ when considering the TEF value.

In comparison, the thermal enhancement factor for the present research is close to the thermal enhancement factor from [30], which presented the V-rib placed on the upper-lower walls of the square duct. However, the maintenance, production, and installation of the current vortex generator are easier than the previous work [30].

Nomenclature

B: Ring height, m
D_h: Hydraulic diameter of channel, m
f: Friction factor
s: Gap spacing between the outer edge of the ISR and duct walls, m
H: Channel height, m
h: Convective heat transfer coefficient, $W \cdot m^{-2} \cdot K^{-1}$
k: Thermal conductivity, $W \cdot m^{-1} \cdot K^{-1}$
Nu: Nusselt number ($=hD_h/k$)
P: Pitch spacing, m
p: Static pressure, Pa
Re: Reynolds number
T: Temperature, K
u_i: Velocity in x_i-direction, $m \cdot s^{-1}$
$\overline{u}$: Mean velocity in the channel, $m \cdot s^{-1}$

Greek letter

TEF: Thermal enhancement factor $(=(Nu/Nu_0)/(f/f_0)^{1/3})$
ρ: Density, $kg \cdot m^{-3}$

Subscript

0: Smooth tube
pp: Pumping power.

Data Availability

No data were used to support this study.

Conflicts of Interest

The authors declare that there are no conflicts of interest regarding the publication of this article.

Acknowledgments

The authors would like to thank Assoc. Prof. Dr. Pongjet Promvonge for suggestions. This research was funded by College of Industrial Technology, King Mongkut's University of Technology North Bangkok (Grant no. Res-CIT0238/2019).

References

[1] M. Bahiraei, N. Mazaheri, Y. Hosseini, and H. Moayedi, "A two-phase simulation for analyzing thermohydraulic performance of Cu–water nanofluid within a square channel enhanced with 90° V-shaped ribs," *International Journal of Heat and Mass Transfer*, vol. 145, Article ID 118612, 2019.

[2] W. Bai, D. Liang, W. Chen, and M. K. Chyu, "Investigation of ribs disturbed entrance effect of heat transfer and pressure drop in pin-fin array," *Applied Thermal Engineering*, vol. 162, Article ID 114214, 2019.

[3] G. Wang, N. Qian, and G. Ding, "Heat transfer enhancement in microchannel heat sink with bidirectional rib," *International Journal of Heat and Mass Transfer*, vol. 136, pp. 597–609, 2019.

[4] P. Liu, J. Lv, F. Shan, Z. Liu, and W. Liu, "Effects of rib arrangements on the performance of a parabolic trough receiver with ribbed absorber tube," *Applied Thermal Engineering*, vol. 156, pp. 1–13, 2019.

[5] Y. Li, Y. Rao, D. Wang, P. Zhang, and X. Wu, "Heat transfer and pressure loss of turbulent flow in channels with miniature structured ribs on one wall," *International Journal of Heat and Mass Transfer*, vol. 131, pp. 584–593, 2019.

[6] W. Bai, W. Chen, L. Yang, and M. K. Chyu, "Numerical investigation on heat transfer and pressure drop of pin-fin array under the influence of rib turbulators induced vortices," *International Journal of Heat and Mass Transfer*, vol. 129, pp. 735–745, 2019.

[7] L. Chai, L. Wang, and X. Bai, "Thermohydraulic performance of microchannel heat sinks with triangular ribs on sidewalls—Part 1: local fluid flow and heat transfer characteristics," *International Journal of Heat and Mass Transfer*, vol. 127, pp. 1124–1137, 2018.

[8] L. Chai, L. Wang, and X. Bai, "Thermohydraulic performance of microchannel heat sinks with triangular ribs on sidewalls—Part 2: average fluid flow and heat transfer characteristics," *International Journal of Heat and Mass Transfer*, vol. 128, pp. 634–648, 2019.

[9] X. Cao, T. Du, Z. Liu, H. Zhai, and Z. Duan, "Experimental and numerical investigation on heat transfer and fluid flow performance of sextant helical baffle heat exchangers," *International Journal of Heat and Mass Transfer*, vol. 142, Article ID 118437, 2019.

[10] A. A. A. Arani and R. Moradi, "Shell and tube heat exchanger optimization using new baffle and tube configuration," *Applied Thermal Engineering*, vol. 157, Article ID 113736, 2019.

[11] M. A. Ismael, "Forced convection in partially compliant channel with two alternated baffles," *International Journal of Heat and Mass Transfer*, vol. 142, Article ID 118455, 2019.

[12] E. M. S. El-Said and M. M. A. Al-Sood, "Shell and tube heat exchanger with new segmental baffles configurations: a comparative experimental investigation," *Applied Thermal Engineering*, vol. 150, pp. 803–810, 2019.

[13] S. W. Chang, T. W. Chen, and Y. W. Chen, "Detailed heat transfer and friction factor measurements for square channel enhanced by plate insert with inclined baffles and perforated slots," *Applied Thermal Engineering*, vol. 159, Article ID 113856, 2019.

[14] A. J. Modi and M. K. Rathod, "Comparative study of heat transfer enhancement and pressure drop for fin-and-circular tube compact heat exchangers with sinusoidal wavy and elliptical curved rectangular winglet vortex generator," *International Journal of Heat and Mass Transfer*, vol. 141, pp. 310–326, 2019.

[15] H. Kobayashi, K. Yaji, S. Yamasaki, and K. Fujita, "Freeform winglet design of fin-and-tube heat exchangers guided by topology optimization," *Applied Thermal Engineering*, vol. 161, Article ID 114020, 2019.

[16] H.-l. Liu, C.-c. Fan, Y.-l. He, and D. S. Nobes, "Heat transfer and flow characteristics in a rectangular channel with combined delta winglet inserts," *International Journal of Heat and Mass Transfer*, vol. 134, pp. 149–165, 2019.

[17] C. Zhai, M. D. Islam, R. Simmons, and I. Barsoum, "Heat transfer augmentation in a circular tube with delta winglet vortex generator pairs," *International Journal of Thermal Sciences*, vol. 140, pp. 480–490, 2019.

[18] M. F. M. Salleh, H. A. Mohammed, and M. A. Wahid, "Thermal and hydraulic characteristics of trapezoidal winglet across fin-and-tube heat exchanger (FTHE)," *Applied Thermal Engineering*, vol. 149, pp. 1379–1393, 2019.

[19] G. Liang, M. D. Islam, N. Kharoua, and R. Simmons, "Numerical study of heat transfer and flow behavior in a circular tube fitted with varying arrays of winglet vortex generators," *International Journal of Thermal Sciences*, vol. 134, pp. 54–65, 2018.

[20] S. Chamoli, R. Lu, J. Xie, and P. Yu, "Numerical study on flow structure and heat transfer in a circular tube integrated with novel anchor shaped inserts," *Applied Thermal Engineering*, vol. 135, pp. 304–324, 2018.

[21] A. Bartwal, A. Gautam, M. Kumar, C. K. Mangrulkar, and S. Chamoli, "Thermal performance intensification of a circular heat exchanger tube integrated with compound circular ring-metal wire net inserts," *Chemical Engineering and Processing-Process Intensification*, vol. 124, pp. 50–70, 2018.

[22] S. Chamoli, R. Lu, D. Xu, and P. Yu, "Thermal performance improvement of a solar air heater fitted with winglet vortex generators," *Solar Energy*, vol. 159, pp. 966–983, 2018.

[23] S. K. Singh, M. Kumar, A. Kumar, A. Gautam, and S. Chamoli, "Thermal and friction characteristics of a circular tube fitted with perforated hollow circular cylinder inserts," *Applied Thermal Engineering*, vol. 130, pp. 230–241, 2018.

[24] S. Chamoli, R. Lu, and P. Yu, "Thermal characteristic of a turbulent flow through a circular tube fitted with perforated vortex generator inserts," *Applied Thermal Engineering*, vol. 121, pp. 1117–1134, 2017.

[25] S. Chamoli, P. Yu, and S. Yu, "Multi-objective shape optimization of a heat exchanger tube fitted with compound inserts," *Applied Thermal Engineering*, vol. 117, pp. 708–724, 2017.

[26] J. S. Sawhney, R. Maithani, and S. Chamoli, "Experimental investigation of heat transfer and friction factor characteristics of solar air heater using wavy delta winglets," *Applied Thermal Engineering*, vol. 117, pp. 740–751, 2017.

[27] S. V. Patankar, C. H. Liu, and E. M. Sparrow, "Fully developed flow and heat transfer in ducts having streamwise-periodic variations of cross-sectional area," *Journal of Heat Transfer*, vol. 99, no. 2, pp. 180–186, 1977.

[28] P. Promvonge, W. Jedsadaratanachai, S. Kwankaomeng, and C. Thianpong, "3D simulation of laminar flow and heat transfer in V-baffled square channel," *International Communications in Heat and Mass Transfer*, vol. 39, no. 1, pp. 85–93, 2012.

[29] Y. Cengel and A. J. Ghajar, *Heat and Mass Transfer: Fundamentals & Applications*, ISBN 978-981-4595-27-8, McGraw-Hill Education, Newyork, NY, USA, 5th edition, 2015.

[30] A. Boonloi and W. Jedsadaratanachai, "Effect of location in transverse plane for 45-degree V-baffle on flow and heat transfer mechanism in a square channel," *Frontiers in Heat and Mass Transfer*, vol. 11, no. 29, 2018.